Hindawi Publishing Corporation
International Journal of Photoenergy
Volume 2012, Article ID 381016, 12 pages
doi:10.1155/2012/381016

Research Article

Modified Grid-Connected CSI for Hybrid PV/Wind Power Generation System

D. Amorndechaphon,[1] S. Premrudeepreechacharn,[1] K. Higuchi,[2] and X. Roboam[3]

[1] *Department of Electrical Engineering, Chiangmai University, Suthep, Muang, Chiangmai 50200, Thailand*
[2] *Department of Electronics Engineering, University of Electro-Communications, 1-5-1 Chofugaoaka, Chofu, Tokyo 182-8585, Japan*
[3] *Laboratoire Plasma et Conversion d'Energie (LAPLACE), Institut National Polytechnique de Toulouse, 31071 Toulouse, France*

Correspondence should be addressed to D. Amorndechaphon, a_damrong@hotmail.com

Received 8 April 2012; Revised 15 August 2012; Accepted 24 August 2012

Academic Editor: Christophe Menezo

The principle of a power conditioning unit for hybrid PV/wind power generation system is proposed. The proposed power conditioner is based on the current source inverter (CSI) topology. All energy sources are connected in parallel with a DC-bus through the modified wave-shaping circuits. To achieve the unity power factor at the utility grid, the DC-link current can be controlled via the wave-shaping circuits with the sinusoidal PWM scheme. In this work, the carrier-based PWM scheme is also proposed to minimize the utility current THD. The power rating of the proposed system can be increased by connecting more PV/wind modules through their wave-shaping circuits in parallel with the other modules. The details of the operating principles, the system configurations, and the design considerations are described. The effectiveness of the proposed CSI is demonstrated by simulation results.

1. Introduction

The steadily increasing energy consumption for the conventional energy sources like a fossil-energy-based fuel has created much interest in the alternative energy sources. Many renewable energy sources are now developed and being widely used. These energy sources can be integrated to form a hybrid system which is an excellent option for distributed energy product. In general, the hybrid systems have better potential to provide higher quality and more reliable power than the single source systems. Recently, the solar and wind energy are the most commonly used renewable energy sources in a hybrid system due to the high efficiency and reliability to supply the continuous power to the load or the utility grid. The typical hybrid power generation system is shown in Figure 1(a). This system includes the energy sources, DC-DC converters, a DC-AC inverter, and the utility grid. All energy sources are connected in parallel to a common DC-AC inverter through their individual DC-DC converters.

Several configurations of hybrid PV/wind power generation systems, applying the various static converter topologies, have been proposed in the literatures [1, 2]. Previous approaches of the hybrid PV/wind power converters were mainly based on voltage source inverter (VSI) topology. One of the commonly used VSI for hybrid PV/wind is shown in Figure 1(b). In this topology, all energy sources are connected to a common DC-bus through the individual DC-DC boost converters. The DC-DC converters are responsible for tracking the maximum power of the wind and PV sources under all operating conditions. The outputs of both DC-DC converters are then connected to a single-phase DC-AC inverter. The DC-link voltage will be regulated by the DC-AC inverter with the current-regulated PWM control to achieve the unity power factor at the utility grid. Nowadays VSI has received a lot of attention but the high switching losses of the switching devices in both conversion stages are still a major drawback of this topology. To overcome this problem, several power converters based on the current source inverter (CSI) topology have been developed [3–8]. Compared with the VSI topology, CSI topology has the ability to boost the output voltage without an additional boost converter [4, 9]. Therefore, CSI is strongly suggested for the grid-connected systems which the magnitude of the DC input voltage is lower than the peak

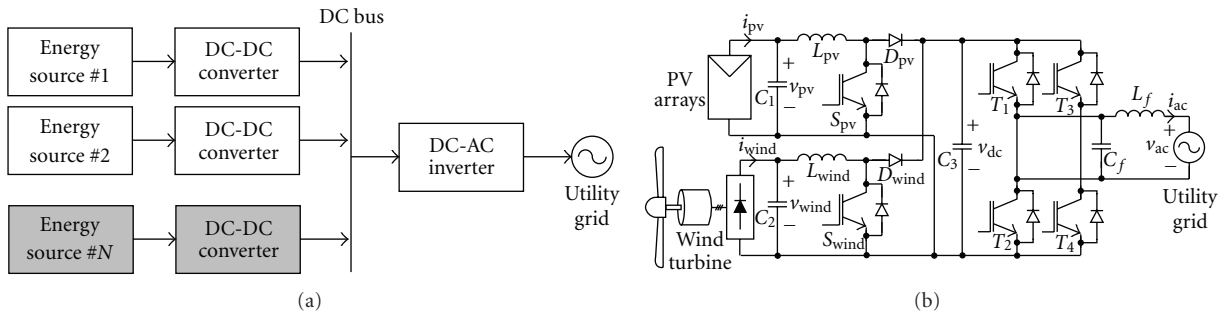

Figure 1: Hybrid PV/wind generation system—(a) general structure of typical hybrid system and (b) hybrid system based on VSI topology.

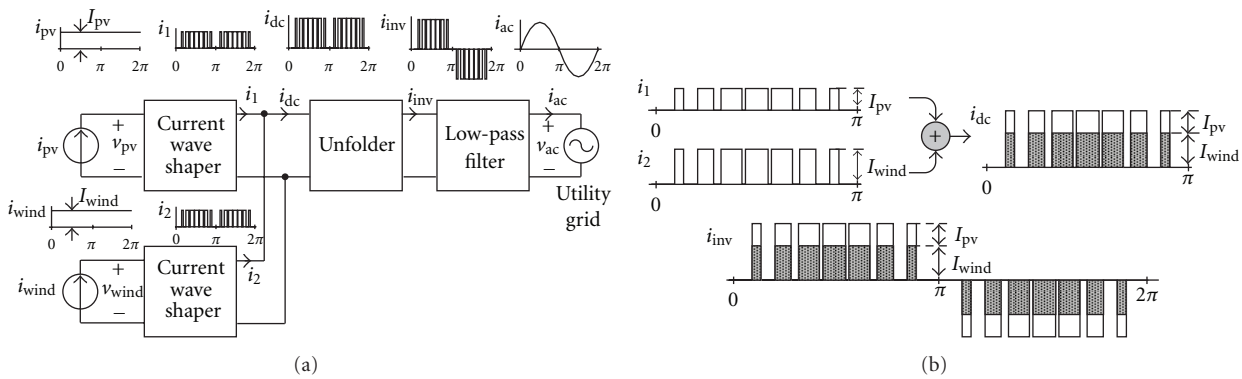

Figure 2: Conceptual expression of the proposed current sharing technique—(a) simplified block diagram and (b) current waveforms for showing the part shared by each energy source.

of utility voltage. In addition, CSI generally features simple converter structure and reliable short-circuit protection. Furthermore, the application of CSI for hybrid PV/wind grid-connected system has not been reported in the previous publications.

In this paper, a modified grid-connected CSI for hybrid renewable energy systems consisting of PV and wind is proposed. The details of the operation principle and the system configuration are also discussed. The simulation setup has been carried out to verify the system performance of the proposed ideas under the different scenarios.

2. Operating Principles

2.1. Overview Concept of the Proposed System with DC-Link Current Sharing Technique. In this section, the overview of the proposed hybrid PV/wind power generation system as shown in Figure 2 can be introduced. The proposed system consists of two constant current sources i_{pv} and i_{wind}, two current wave-shaping circuits (can be named as DC-DC chopper), an unfolding circuit, and a low-pass filter. Two constant current sources are connected in parallel to a common DC-bus through their own current wave-shaping circuits. Both wave shaping circuits, operating in the same switching frequency, are used to perform the PWM output currents i_1 and i_2 at a DC-bus. In order to supply active power to the utility grid, the DC-link current i_{dc} is controlled to be in phase with the utility voltage v_{ac}. Therefore, the unity power factor can be achieved. The unfolding circuit is used to produce a unipolar pulse-width modulation (PWM) current i_{inv} by setting the direction of a PWM current i_{dc} at a DC link. At the last stage, low-pass filter is connected to eliminate the high-frequency harmonic components in a unipolar PWM current i_{inv} before injected to the utility grid.

In Figure 2(b), the waveforms of i_1, i_2, i_{dc}, and i_{inv} in the block diagram in Figure 2(a) are shown. According to Kirchhoff's current law (KCL), it can be seen that the PWM current at a DC-bus i_{dc} is the sum of output currents from the two wave-shaping circuits i_1 and i_2, respectively. Hence, the instantaneous DC-link current i_{dc} can be determined by $i_{dc} = i_1 + i_2$. In addition, the magnitude of i_{dc} can be found by summing the magnitude of i_1 and i_2 ($I_{dc} = I_{pv} + I_{wind}$), respectively. As a result, the magnitude of i_{dc} can be independently controlled by two constant current sources i_{pv} and i_{wind}, respectively.

2.2. Circuit Configuration and Control Strategy. Figure 3(a) shows the circuit topology of the proposed grid-connected CSI for hybrid PV/wind power generation. The circuit diagram differs from that of a VSI in Figure 1(b) by the absence of a DC-link capacitor C_3. The proposed circuit is composed of two wave-shaping circuits, a thyristor-based H-bridge inverter, and *CL* low-pass filter. Input renewable energy sources, PV and wind, are connected to a common DC-bus through their own wave-shaping circuits. The proposed system control scheme is also illustrated in Figure 3(b).

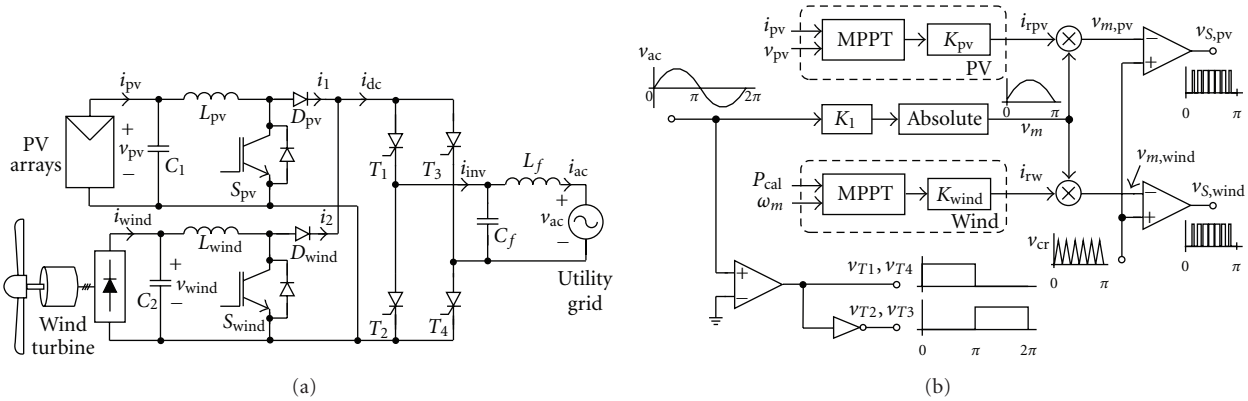

(a) (b)

Figure 3: Proposed grid-connected CSI for hybrid PV/wind power generation—(a) power converter scheme and (b) system control scheme.

On the DC-side of the inverter, the DC chokes L_{pv} and L_{wind} are required to provide the smooth and continuous DC currents i_{pv} and i_{wind}, respectively. Chopper switches S_{pv} and S_{wind} can be controlled to shape the constant input DC current i_{pv} and i_{wind} to be the PWM currents i_1 and i_2, respectively, at a DC-bus. To achieve the unity power factor at the utility grid, the utility current i_{ac} is required to be sinusoidal and in phase with the utility voltage v_{ac}. Thus the voltage v_{ac} will be rectified to establish a full-wave rectified sinusoidal signal v_m, where K_1 is an absolute gain. In the same time, the maximum power point tracker (MPPT) can be used for tracking the maximum power of PV and wind by multiplying the reference signal v_m with the MPPT reference of each energy source i_{rpv} and i_{rw} to produce the modulating signal $v_{m,pv}$ and $v_{m,wind}$, respectively. In PV array, an MPPT algorithm is used to determine the optimal operating point i_{rpv}. The optimal current i_{rpv} is calculated and tracked from measured valued of PV voltage v_{pv} and PV current i_{pv}. Similarly, for the wind turbine, the extracted power of the wind turbine P_{cal} and wind speed ω_m are measured. The optimal point i_{rw} can be provided by the MPPT controller. In both energy sources, K_{pv} and K_{wind} are the constant gain of the MPPT controller of PV and wind, respectively.

To obtain the control signal of chopper switches $v_{S,pv}$ and $v_{S,wind}$, the modulating signals $v_{m,pv}$ and $v_{m,wind}$ are compared with a triangular-shaped carrier waveform v_{cr} of the switching frequency f_{sw}. The instantaneous DC-link current i_{dc} can be obtained by the summation of i_1 and i_2. The H-bridge inverter operates in synchronism with the utility grid and is controlled to provide a unipolar PWM current i_{inv}. The zero-crossing circuit is used to generate the control signal of H-bridge inverter v_{T1}, v_{T2}, v_{T3}, and v_{T4}. Switches T_1 and T_4 are turned on in the positive half-cycle of the grid voltage v_{ac}, whereas T_2 and T_3 are turned on in the negative half cycle. It can be observed that the inverter current i_{inv} is obtained by unfolding the DC-link current i_{dc}. At the last stage, C_f and L_f form the low-pass filter which attenuates the high frequency components in the inverter output current i_{inv}.

The principle of the PWM scheme for the proposed CSI is illustrated in Figure 4. For the proposed modulation scheme, two modulating waves $v_{m,pv}$ and $v_{m,wind}$ are required. Both modulating waves are of the same frequency and synchronize with the utility grid but the magnitudes $V_{m,pv}$ and $v_{m,wind}$ are different. The modulating waves $v_{m,pv}$ and $v_{m,wind}$ are compared with a common triangular carrier wave v_{cr}, generating two gating signals $v_{S,pv}$ and $v_{S,wind}$ for chopper switches S_{pv} and S_{wind}, respectively. It should be noted that the fundamental-frequency component of the inverter current i_{inv} can be expressed as i_{inv1} as shown in Figure 4.

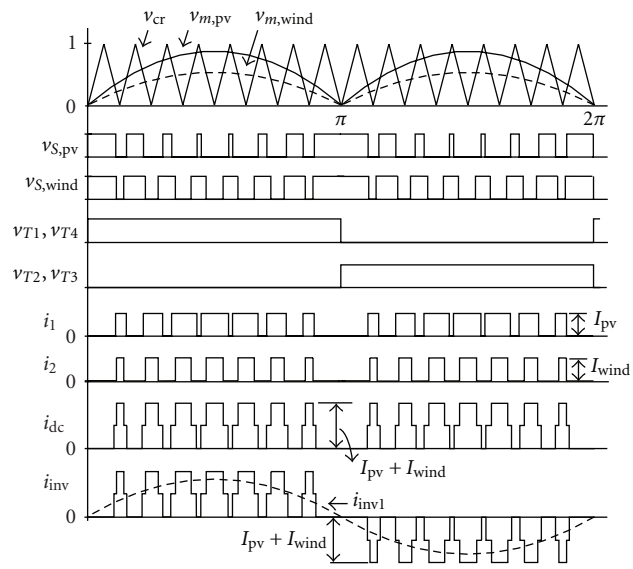

Figure 4: Steady-state waveforms of the proposed grid-connected CSI for hybrid PV/wind system.

2.3. Inverter Mode of Operation. In order to understand the operation details of the proposed grid-connected CSI in Figure 3(a), the equivalent circuit is illustrated in Figure 5. This circuit can be subdivided into two configurations, the input DC-side and the output AC-side, respectively.

For a simplify analysis in each interval of the circuit, the following conditions are assumed.

(I) The input voltage sources v_{pv} and v_{wind} and DC chokes L_{pv} and L_{wind} can be considered and modeled

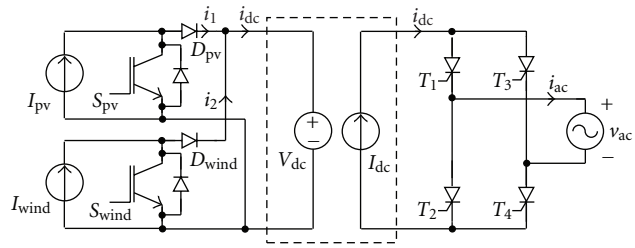

Figure 5: Simplified equivalent circuit of the proposed system.

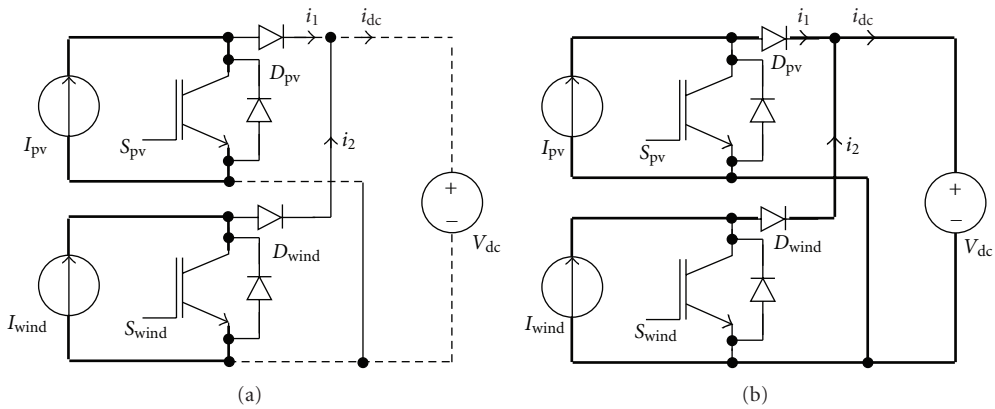

Figure 6: DC-side operation—(a) $v_m < v_{cr}$ and (b) $v_m > v_{cr}$.

as the constant current sources I_{pv} and I_{wind}, respectively.

(II) The output voltage at the DC-side can be assumed to be a constant DC voltage source V_{dc}.

(III) The input current at the AC-side can be assumed to be a constant DC current source I_{dc}.

(IV) All semiconductor switches in the DC-side and the AC-side are operated at the switching frequency (f_{sw}) and the grid frequency (f_{line}), respectively.

2.3.1. DC-Side Operation. For the one switching period, the operation of the converter in the DC-side can be divided into two stages. The equivalent circuit for each stage is shown in Figure 6 and its key waveforms are depicted in Figure 4. Assuming that the modulating signals for energy sources can be defined as $v_{m,pv} = v_{m,wind} = v_m$. The operation processes of the DC-side are specified as follows.

Stage 1 ($v_m < v_{cr}$). When $v_m < v_{cr}$, chopper switches S_{pv} and S_{wind} are on, chopper diodes D_{pv} and D_{wind} are off, the input DC currents I_{pv} and I_{wind} flow through S_{pv} and S_{wind}, respectively. The current I_{pv} and I_{wind} cannot flow through the diodes D_{pv} and D_{wind}, leading to $i_1 = i_2 = 0$. According to KCL, the DC-link current i_{dc} can be considered as consisting of the sum of diode currents i_1 and i_2. That is,

$$i_{dc}(t) = 0. \tag{1}$$

Stage 2 ($v_m > v_{cr}$). When $v_m > v_{cr}$, chopper switches S_{pv} and S_{wind} are off, chopper diodes D_{pv} and D_{wind} are on, the input DC currents I_{pv} and I_{wind} flow to the load through D_{pv} and D_{wind}, respectively, resulting in $i_1 = I_{pv}$ and $i_2 = I_{wind}$. Similar to the first stage, the DC-link current i_{dc} is obtained as

$$i_{dc}(t) = I_{pv} + I_{wind}. \tag{2}$$

The DC-link current i_{dc} for all stages can be rewritten in term of the switching states as follows:

$$i_{dc}(t) = I_{pv}\left[1 - d_{pv}\right] + I_{wind}[1 - d_{wind}], \tag{3}$$

where d_{pv} and d_{wind} are the switching states of the chopper switches S_{pv} and S_{wind}, respectively. The switching states $d_{pv} = 1$ and $d_{wind} = 1$ if $v_m < v_{cr}$ (in stage 1); otherwise 0 (in stage 2).

2.3.2. AC-Side Operation. In Figure 7, the equivalent circuit in the AC-side is shown. The AC utility voltage can be expressed by $v_{ac} = V_{ac} \cdot \sin(\omega t)$, where V_{ac} is the peak of utility voltage. The operation of this side consists of two stages during the switching cycle. The operation can be described as follows.

Stage 1 ($v_{ac} > 0$). When $v_{ac} > 0$, the inverter switches T_1 and T_4 are on, T_2 and T_3 are off, the input DC current I_{dc} flows to the grid through T_1 and T_4, respectively. Then the AC utility current i_{ac} equals to I_{dc}.

Stage 2 ($v_{ac} < 0$). The inverter switches T_1 and T_4 are off, T_2 and T_3 are on, when $v_{ac} < 0$. The DC current I_{dc} flows to the grid through T_2 and T_3, respectively, resulting in the utility current i_{ac} to be equal to $-I_{dc}$.

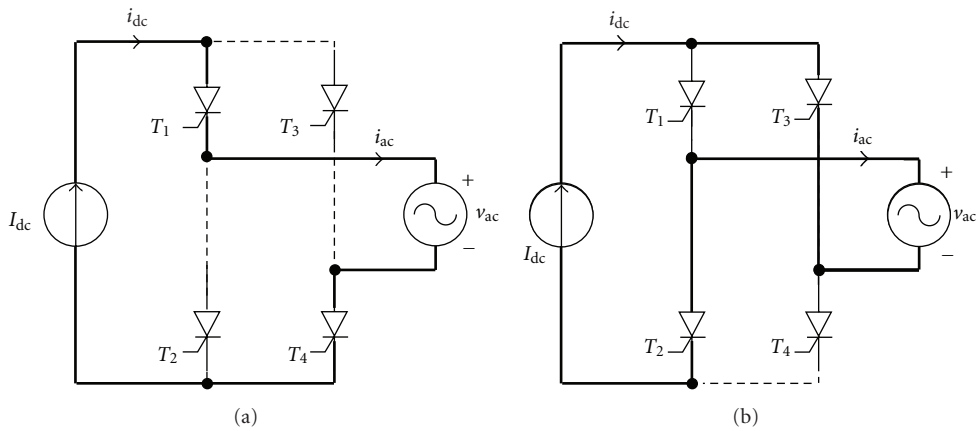

Figure 7: AC-side operation—(a) $v_{ac} > 0$ and (b) $v_{ac} < 0$.

Therefore, the utility current i_{ac} can be defined as

$$i_{ac}(t) = \begin{cases} i_{dc}(t); & \sin(\omega t) \geq 0 \\ -i_{dc}(t); & \sin(\omega t) < 0. \end{cases} \tag{4}$$

It should be noted that the low-pass filter is not considered in this analysis. Hence, the PWM output current i_{inv} is equal to the utility current i_{ac} ($i_{inv} = i_{ac}$).

2.4. PWM Current Analysis. From the PWM scheme in Section 2.2, the analysis of harmonic components in the proposed CSI can be performed. The mathematical expression of the PWM currents i_1 and i_2 can generally be expressed as follows [3]:

$$\begin{aligned} i_1(t) &= \frac{m_{pv} I_{pv}}{2} \cdot |\sin(\omega t)| \\ &\quad + \sum_{k=1}^{\infty} \frac{I_{pv}}{\pi k} \cdot \sin\left[k\pi m_{pv} |\sin(\omega t)|\right] \cdot \cos(k\omega_s t). \\ i_2(t) &= \frac{m_{wind} I_{wind}}{2} \cdot |\sin(\omega t)| \\ &\quad + \sum_{k=1}^{\infty} \frac{I_{wind}}{\pi k} \cdot \sin[k\pi m_{wind} |\sin(\omega t)|] \cdot \cos(k\omega_s t), \end{aligned} \tag{5}$$

where k = the number of kth harmonic component; $\omega \ll \omega_s$; $\omega = 2\pi f_{line}$ and $\omega_s = 2\pi f_{sw}$; $m_{pv} = V_{m,pv}/V_{cr}$ and $m_{wind} = V_{m,wind}/V_{cr}$; m_{pv} and m_{wind} are the modulation index of PV and wind sources, respectively; $V_{m,pv}$ and $V_{m,wind}$ are the peaks of modulating signals for PV and wind sources $v_{m,pv}$ and $v_{m,wind}$, respectively; V_{cr} is the peak of the triangular carrier waveform v_{cr}. Equations (5) are valid to $0 \leq m_{pv} \leq 1$ and $0 \leq m_{wind} \leq 1$, respectively.

The DC-link current i_{dc} can be found from

$$i_{dc}(t) = i_1(t) + i_2(t). \tag{6}$$

Thus,

$$\begin{aligned} i_{dc}(t) &= \frac{1}{2}\left(m_{pv} I_{pv} + m_{wind} I_{wind}\right) \cdot |\sin(\omega t)| \\ &\quad + \sum_{k=1}^{\infty} \frac{I_{pv}}{\pi k} \cdot \sin\left[k\pi m_{pv} |\sin(\omega t)|\right] \cdot \cos(k\omega_s t) \\ &\quad + \sum_{k=1}^{\infty} \frac{I_{wind}}{\pi k} \cdot \sin[k\pi m_{wind} |\sin(\omega t)|] \cdot \cos(k\omega_s t). \end{aligned} \tag{7}$$

According to (4) the inverter output current i_{inv} can be obtained by the operating of the unfolding circuit. Hence, the inverter output current i_{inv} can be expressed in terms of its harmonic components as

$$\begin{aligned} i_{inv}(t) &= \frac{1}{2}\left(m_{pv} I_{pv} + m_{wind} I_{wind}\right) \cdot \sin(\omega t) \\ &\quad + \sum_{k=1}^{\infty} \frac{I_{pv}}{\pi k} \cdot \sin\left[k\pi m_{pv} \sin(\omega t)\right] \cdot \cos(k\omega_s t) \\ &\quad + \sum_{k=1}^{\infty} \frac{I_{wind}}{\pi k} \cdot \sin[k\pi m_{wind} \sin(\omega t)] \cdot \cos(k\omega_s t). \end{aligned} \tag{8}$$

Under the conditions of $I_{pv} = I_{wind}$ and $m_{pv} \neq m_{wind}$, the waveform of the inverter output current i_{inv} and its harmonic contents in (8) can be shown in Figure 8. It can be observed that the waveform of the inverter current i_{inv} is close to a unipolar PWM waveform. We can consider at the conditions of $I_{pv} = I_{wind} = I$ and $m_{pv} = m_{wind} = m$, the current i_{inv} simplified as follows:

$$\begin{aligned} i_{inv}(t) &= mI \cdot \sin(\omega t) \\ &\quad + \sum_{k=1}^{\infty} \frac{2I}{\pi k} \cdot \sin[k\pi m \sin(\omega t)] \cdot \cos(k\omega_s t). \end{aligned} \tag{9}$$

From this result, the PWM inverter current i_{inv} can be shown in Figure 9(a). This waveform is similar to a unipolar PWM waveform. Figure 9(b) shows the harmonic spectrum of the inverter current i_{inv}. It can be seen that the current has

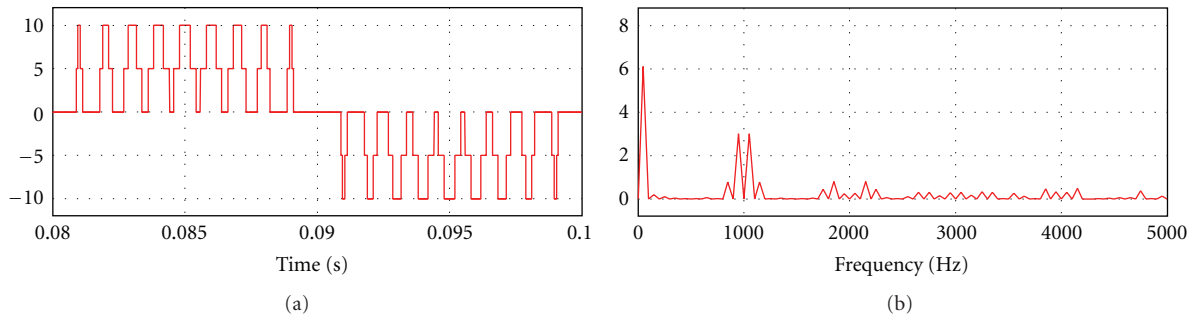

Figure 8: PWM output current waveform i_{inv} and harmonic content of the proposed circuit operating at $m_{\text{pv}} \neq m_{\text{wind}}$, $I_{\text{pv}} = I_{\text{wind}}$, $f_{\text{line}} = 50\,\text{Hz}$ and $f_{\text{sw}} = 1\,\text{kHz}$.

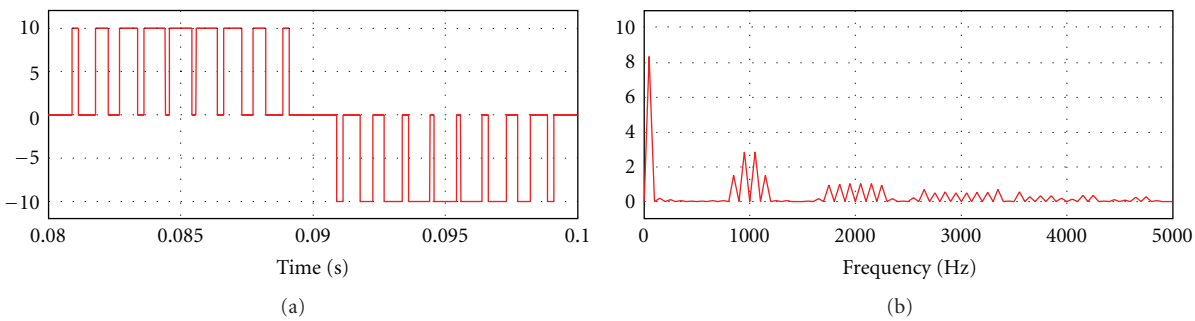

Figure 9: PWM output current waveform i_{inv} and harmonic content of the proposed circuit operating at $m_{\text{pv}} = m_{\text{wind}}$, $I_{\text{pv}} = I_{\text{wind}}$, $f_{\text{line}} = 50\,\text{Hz}$, and $f_{\text{sw}} = 1\,\text{kHz}$.

harmonics at the multiples of the switching frequency, that is, at f_{sw}, $2f_{\text{sw}}$, and so on. The harmonics of significant magnitudes also appear in the side bands of the switching frequency and its multiples.

2.5. Carrier-Based PWM Scheme. In order to reduce the harmonic distortion in the inverter output current i_{inv}, a carrier-based PWM scheme can be proposed. In general, this scheme can be classified into two categories: phase-shifted and level-shifted modulations. In this paper, a phase-shifted modulation is only studied and applied to the proposed hybrid PV/wind power systems. Normally, the hybrid PV/wind system may be connected in parallel more than two energy sources. The n energy sources require n triangular carrier signals. For the phase-shifted multicarrier modulation, the carrier waves for each module $v_{\text{cr,pv}}$ and $v_{\text{cr,wind}}$ are of same amplitude and frequency, but there is a phase shift ϕ_{cr} between any the adjacent carrier waves, given by

$$\phi_{\text{cr}} = \frac{360^\circ}{n}. \tag{10}$$

For the proposed hybrid PV/wind system as shown in the Figure 3(a), there are two energy sources for system. The modulating signals $v_{m,\text{pv}}$ and $v_{m,\text{wind}}$ have the same frequency but the amplitude is different depending on the MPPT signals of each module. According to (10), the phase shift ϕ_{cr} between each carrier wave $v_{\text{cr,pv}}$ and $v_{\text{cr,wind}}$ is 180°. The gate signals $v_{S,\text{pv}}$ and $v_{S,\text{wind}}$ are generated by comparing

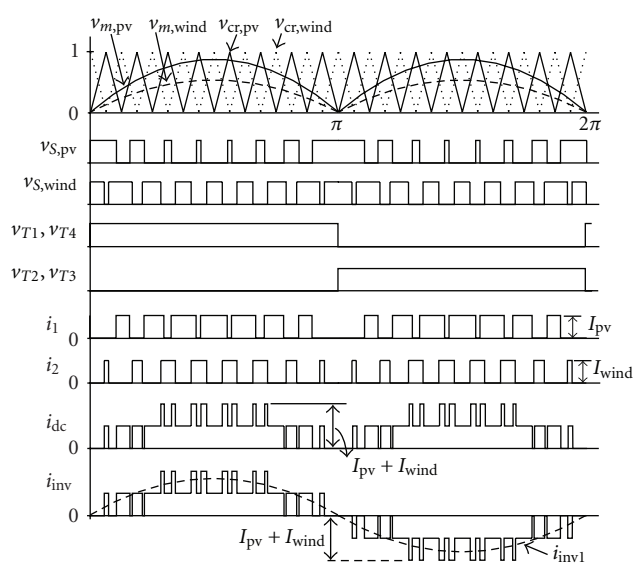

Figure 10: The steady-state waveforms of the proposed phase-shifted PWM multicarrier modulation.

the modulating wave $v_{m,\text{pv}}$ and $v_{m,\text{wind}}$ with the carrier waves $v_{\text{cr,pv}}$ and $v_{\text{cr,wind}}$, respectively. The principle of the proposed phase-shifted modulation for the hybrid PV/wind system can be shown in Figure 10. The inverter operates under the conditions of $I_{\text{pv}} = I_{\text{wind}} = I$ and $m_{\text{pv}} = m_{\text{wind}} = m$.

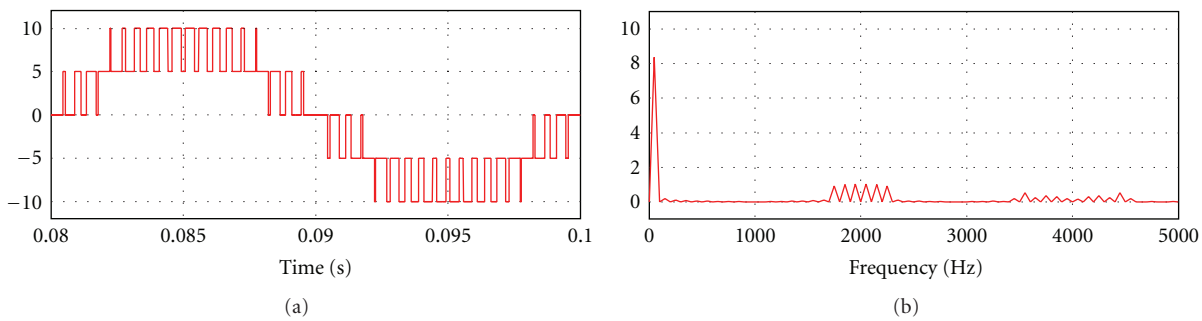

Figure 11: PWM output current waveform i_{inv} and harmonic content of the proposed circuit with phase-shifted modulation operating at $I_{\text{pv}} = I_{\text{wind}}$, $m_{\text{pv}} = m_{\text{wind}}$, $f_{\text{line}} = 50\,\text{Hz}$, and $f_{\text{sw}} = 1\,\text{kHz}$.

The inverter PWM current i_{inv} can be expressed in terms of Fourier series as [3]

$$i_{\text{inv}}(t) = mI \cdot \sin(\omega t) + \sum_{\text{even } k} \frac{2I}{\pi k} \cdot \sin[k\pi m \sin(\omega t)] \cdot \cos(k\omega_s t). \tag{11}$$

The inverter output current waveform i_{inv} based on phase-shifted multicarrier modulation is shown in Figure 11(a), and its spectrum is also illustrated in Figure 11(b). The operating conditions are $I_{\text{pv}} = I_{\text{wind}} = I$, $m_{\text{pv}} = m_{\text{wind}} = m$, $f_{\text{line}} = 50\,\text{Hz}$, and $f_{\text{sw}} = 1\,\text{kHz}$. The inverter current has harmonics and sidebands at the multiple of the twice switching frequency, that is, $2f_{\text{sw}}$, $4f_{\text{sw}}$, and so on. It is clear that the current waveform is formed by five current steps: $2I$, I, 0, $-I$, and $-2I$, resulting in a further reduction in THD.

3. Design Consideration

3.1. Input DC Choke Design. Large inductors L_{pv} and L_{wind} are used in the DC-side of the inverter, which make the input voltage sources v_{pv} and v_{wind} appear as the constant DC current sources I_{pv} and I_{wind}. When the chopper switch is turned on, the inductor current rises and the energy is stored in the inductor. If switch is turned off, the energy stored in the inductor is transferred to the AC-side through the diode and the inductor current falls. To design the value of this inductor, the inductor stored energy must be considered. When the switch is turned on, the energy stored in the inductor is

$$E_L = \frac{1}{2} L I^2 = P_{\text{dc}} T_{\text{on}}, \tag{12}$$

where L = choke inductance, P_{dc} = average input power at DC-side, T = switching period, $T_{\text{on}} = T/2$ = turn-on time, and I = average input current. The choke inductance can be expressed as

$$L = \frac{P_{\text{ac}}}{\eta I^2 f_{\text{sw}}}, \tag{13}$$

where η = converter efficiency, $P_{\text{ac}} = \eta \cdot P_{\text{dc}}$ = average output power at AC-side, and f_{sw} = switching frequency.

Table 1: Simulation parameters.

Output-rated power	$P_{\text{ac}} = 1000\,\text{W}$
PV source current	$I_{\text{pv}} = 5\,\text{A}$
Wind source current	$I_{\text{wind}} = 5\,\text{A}$
Utility grid voltage	$v_{\text{ac}} = 220\,\text{V}_{\text{rms}}$
Utility grid frequency	$f_{\text{line}} = 50\,\text{Hz}$
Chopper switching frequency	$f_{\text{sw}} = 3\,\text{kHz}$
Input inductor for PV converter	$L_{\text{pv}} = 13\,\text{mH}$
Input inductor for wind converter	$L_{\text{wind}} = 13\,\text{mH}$
Low-pass filter inductor	$L_f = 4\,\text{mH}$
Low-pass filter capacitor	$C_f = 2\,\mu\text{F}$

3.2. Output Low-Pass Filter Design. In order to reduce the high-frequency harmonics in the PWM output current i_{inv} of the grid-connected inverter, a low-pass filter is needed. Passive low-pass filters are normally used as L, LC, CL, and LCL filters. In this paper, a simple CL low-pass filter is chosen. A detailed analysis is not considered in this paper. Following the design procedure of [10], the inductor L_f and capacitor C_f can be found through the following equations:

$$L_f = \frac{V_{\text{ac}}}{P_{\text{ac}} 2\pi f_{\text{sw}}}, \qquad C_f = \frac{0.33}{2\pi f_{\text{sw}} L_f}, \tag{14}$$

where V_{ac} is the amplitude of the grid voltage v_{ac}.

4. Results and Discussion

To verify the proposed grid-connected CSI for hybrid PV/wind system with a simple current-sharing technique, the simulation setup has been designed and carried out with PSIM. It should be noted that the MPPT operating for PV and wind energy is not studied in this paper. The circuit parameters are shown in Table 1. The PV and wind energy sources v_{pv} and v_{wind} and input DC chokes L_{pv} and L_{wind} are modeled by DC current sources I_{pv} and I_{wind}, respectively.

Figure 12 confirms the principle of PWM strategy for the proposed CSI operating under the condition of $m_{\text{pv}} = 0.9$ and $m_{\text{wind}} = 0.4$. The gate signals for all switches in CSI $v_{S,\text{pv}}$,

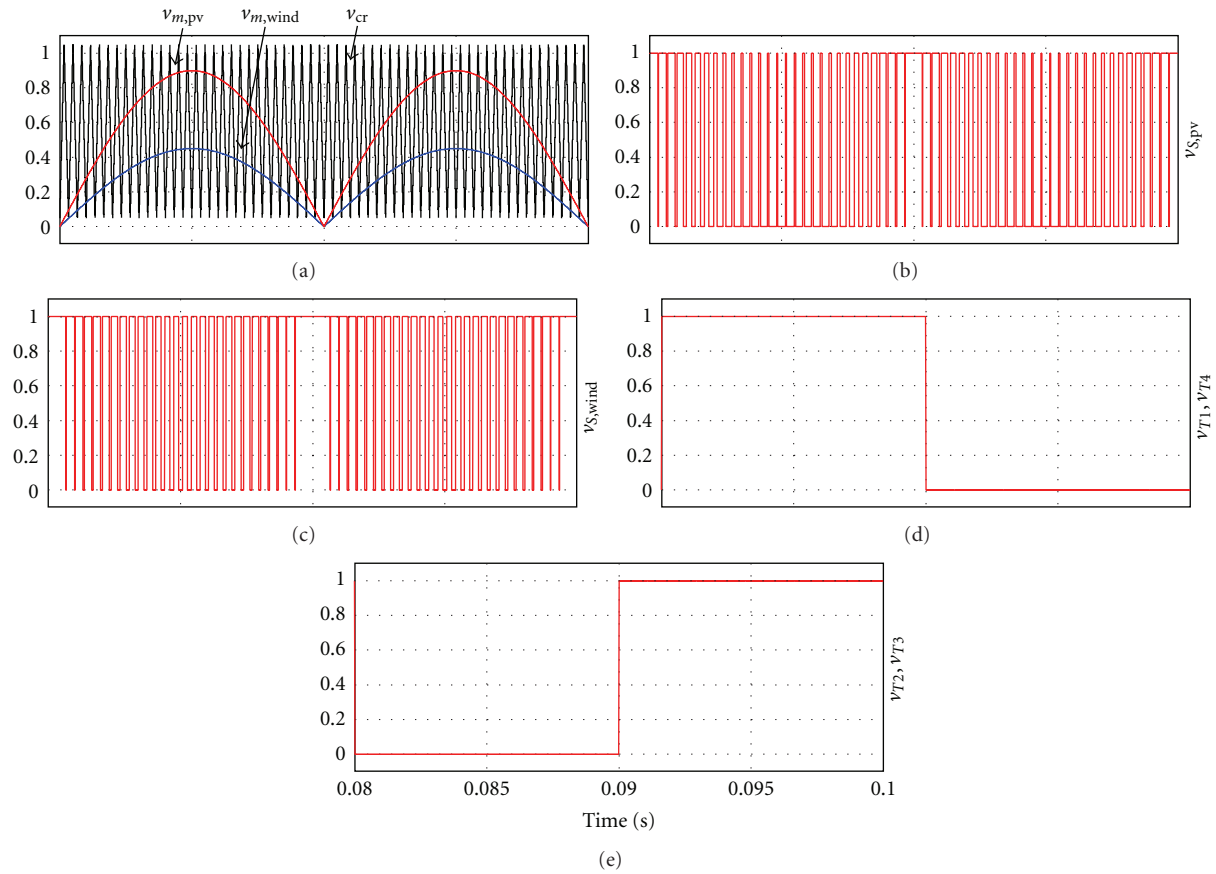

Figure 12: PWM switching strategy (top to bottom) $v_{m,\mathrm{pv}}$, $v_{m,\mathrm{wind}}$, v_{cr}, $v_{S,\mathrm{pv}}$, $v_{S,\mathrm{wind}}$, v_{T1}, v_{T4}, v_{T2}, and v_{T3}.

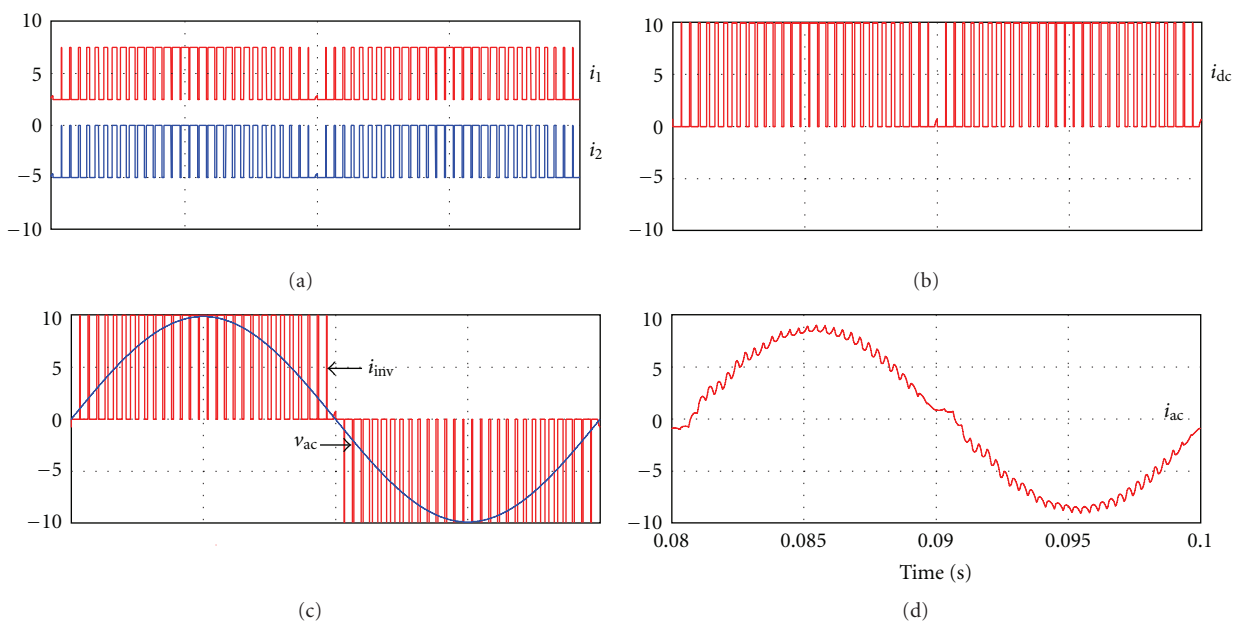

Figure 13: Operation of the system under the conditions of $m_{\mathrm{pv}} = m_{\mathrm{wind}}$, $I_{\mathrm{pv}} = I_{\mathrm{wind}}$, $f_{\mathrm{line}} = 50\,\mathrm{Hz}$ and $f_{\mathrm{sw}} = 3\,\mathrm{kHz}$ (top to bottom) i_1, i_2, i_{dc}, i_{inv}, v_{ac}, and i_{ac}.

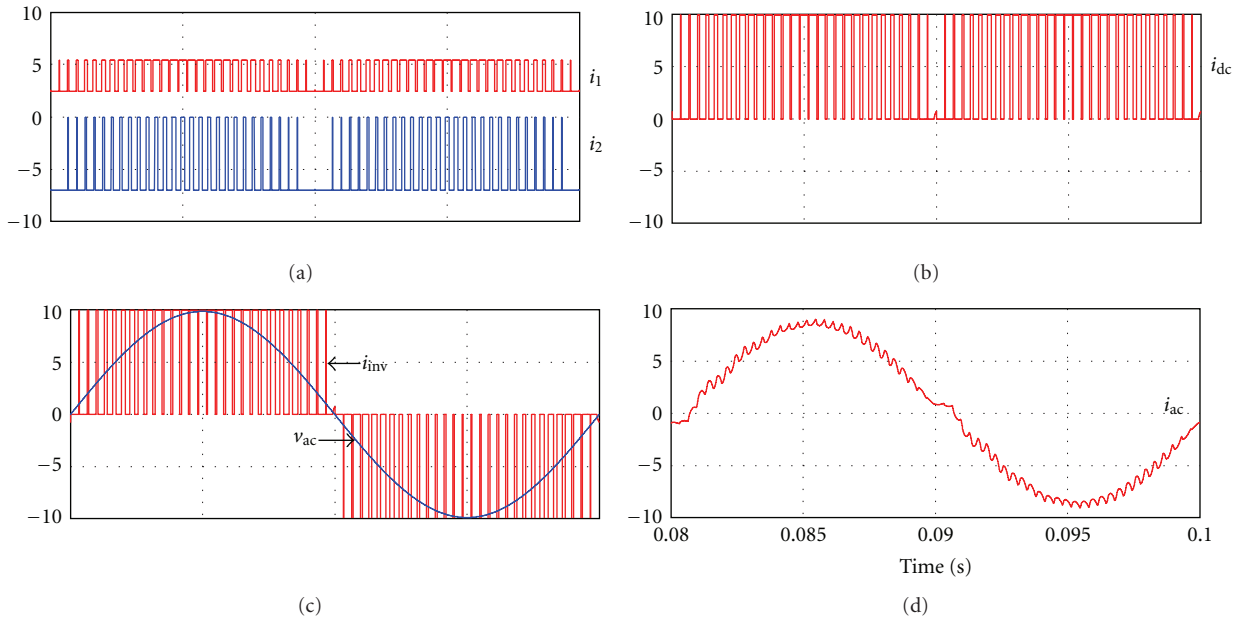

FIGURE 14: Operation of the system under the conditions of $m_{pv} = m_{wind}$, $I_{pv} < I_{wind}$, $f_{line} = 50$ Hz and $f_{sw} = 3$ kHz (top to bottom) i_1, i_2, i_{dc}, i_{inv}, v_{ac}, and i_{ac}.

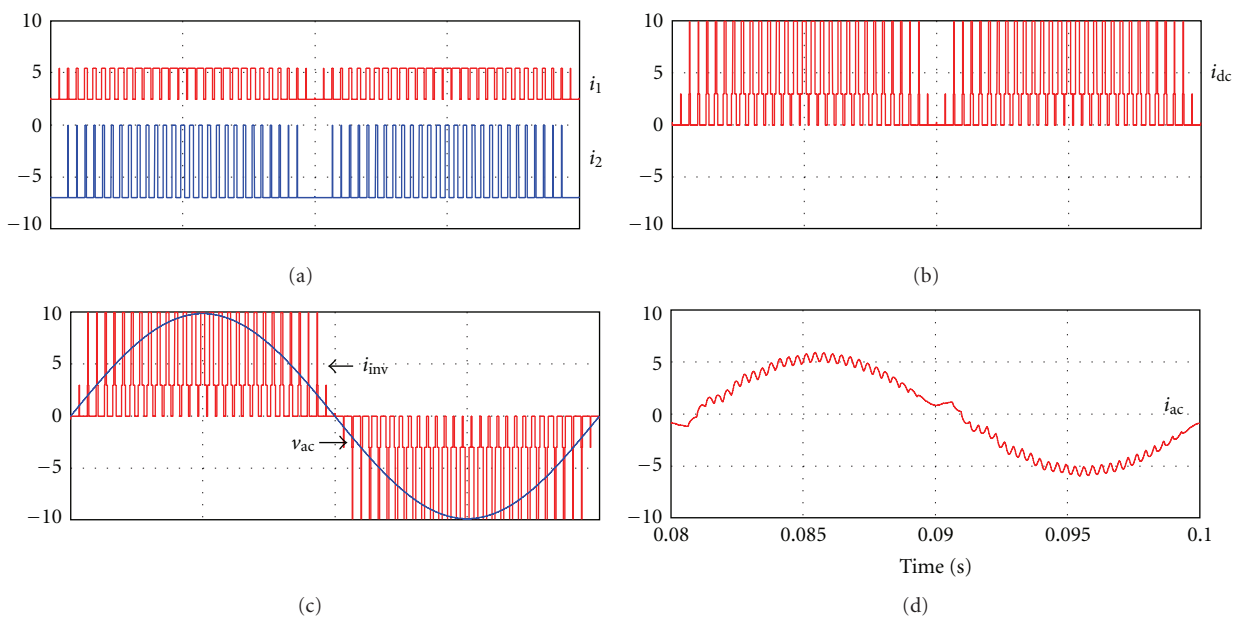

FIGURE 15: Operation of the system under the conditions of $m_{pv} > m_{wind}$, $I_{pv} < I_{wind}$, $f_{line} = 50$ Hz and $f_{sw} = 3$ kHz (top to bottom) i_1, i_2, i_{dc}, i_{inv}, v_{ac}, and i_{ac}.

$v_{S,wind}$, v_{T1}, v_{T2}, v_{T3}, and v_{T4} are also shown in Figure 12. Figures 13, 14 and 15 show the simulated waveform for the proposed CSI, operating under the different conditions, (a) $m_{pv} = m_{wind}$ and $I_{pv} = I_{wind}$; (b) $m_{pv} = m_{wind}$ and $I_{pv} < I_{wind}$; (c) $m_{pv} > m_{wind}$ and $I_{pv} < I_{wind}$. The following can be observed.

(a) The two different currents i_1 and i_2 can be combined to produce the current i_{dc} at a DC-bus.

(b) The amplitude of i_{dc} can be determined by $I_{DC} = I_{pv} + I_{wind}$. The magnitude of i_1 and i_2 can be independently controlled by the output power of each energy source.

(c) The unfolding circuit has two complementary switch pairs (T_1, T_4 and T_2, T_3) switching at line frequency 50 Hz. The unipolar PWM current i_{inv} is performed by unfolding the DC-link current i_{dc}.

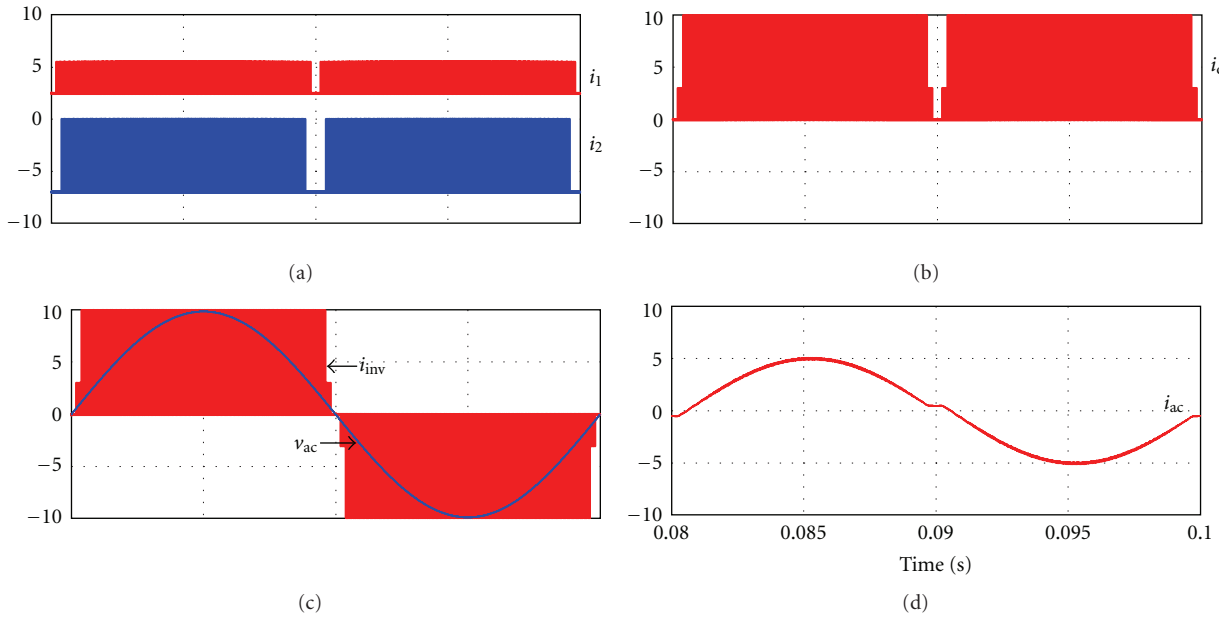

Figure 16: Operation of the system under the conditions of $m_{pv} > m_{wind}$, $I_{pv} < I_{wind}$, $f_{line} = 50$ Hz and $f_{sw} = 20$ kHz (top to bottom) i_1, i_2, i_{dc}, i_{inv}, and i_{ac}.

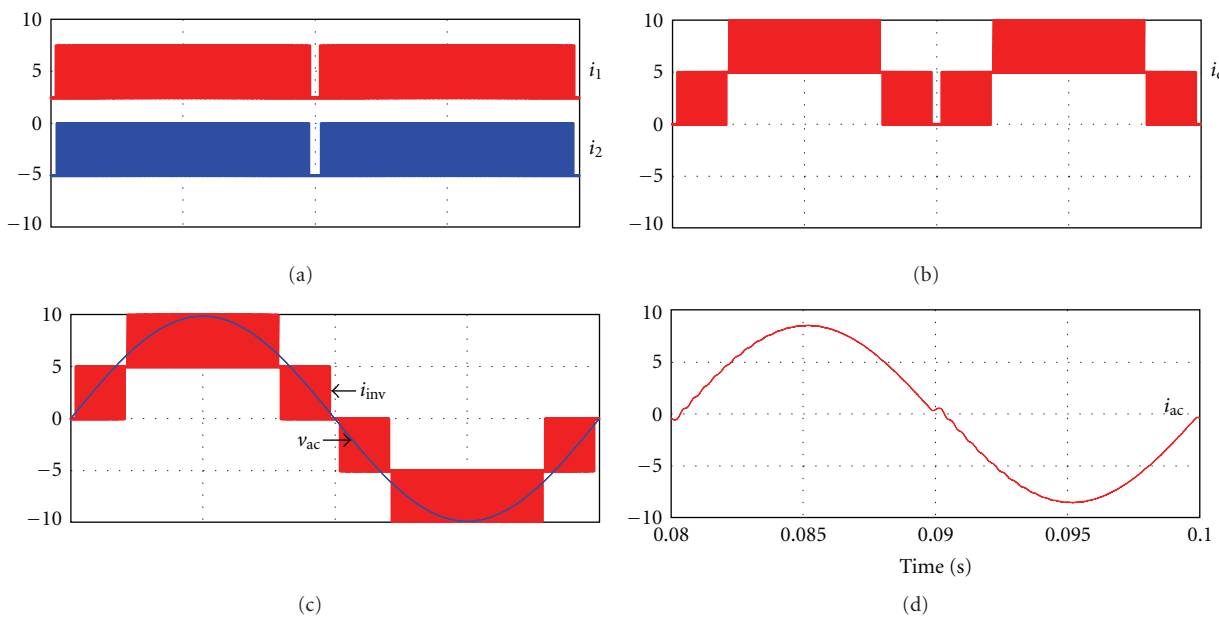

Figure 17: Simulated waveforms of the hybrid PV/wind system with phase-shifted PWM operating under the conditions of $m_{pv} = m_{wind}$, $I_{pv} = I_{wind}$, $f_{line} = 50$ Hz and $f_{sw} = 20$ kHz (top to bottom) i_1, i_2, i_{dc}, i_{inv}, v_{ac}, and i_{ac}.

(d) The waveform of the grid current i_{ac} is close to sinusoidal with low THD. The low amount of harmonic distortion is due to the elimination of high-order harmonic contents by the filtering effect of *CL* low-pass filter.

Figure 16 shows the simulated waveforms for the proposed CSI, operating at higher switching frequency. It can be observed that the proposed converter can produce a smooth AC current at the utility grid with low harmonic components. The waveforms of the proposed grid-connected CSI for hybrid PV/wind system with phase-shifted multicarrier modulation are shown in Figure 17. It can be noted that the inverter output current waveform i_{inv} is formed with five current levels.

In higher power applications, the increasing of output power rating of a hybrid PV/wind power generation system is required. It can be achieved by connecting more PV/wind

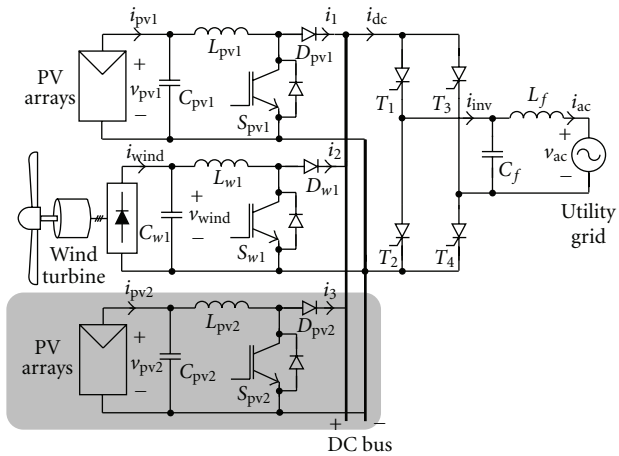

Figure 18: Extension energy sources for increasing the output power of the proposed hybrid PV/wind system.

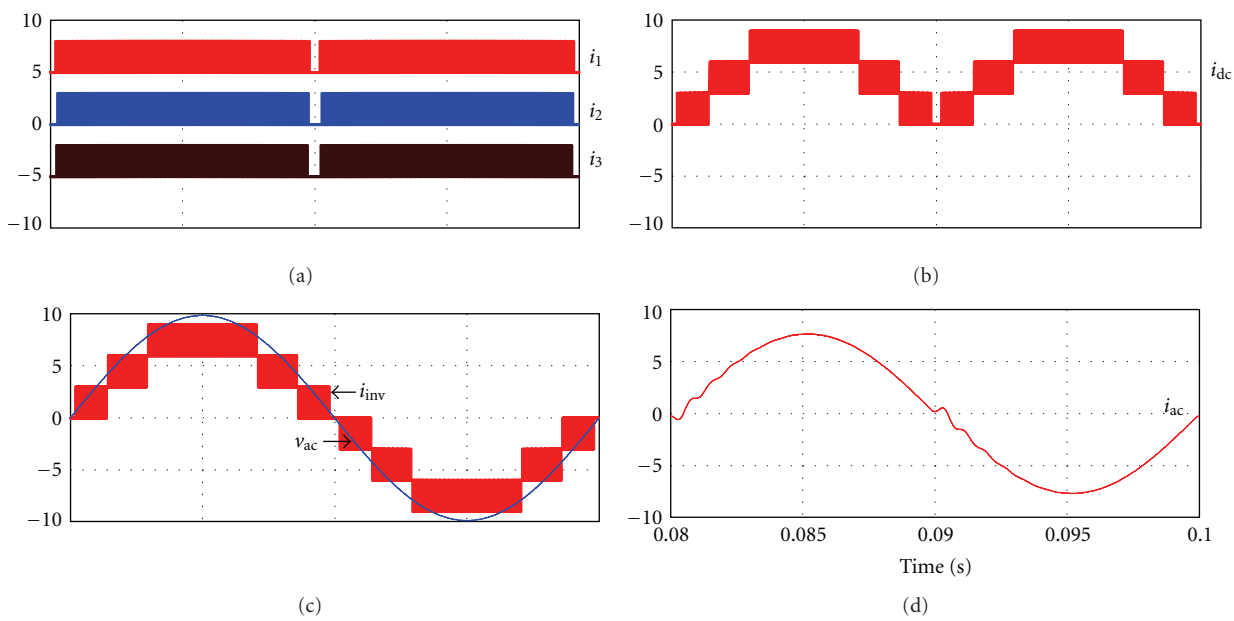

Figure 19: Simulated waveforms of the multimodules hybrid PV/wind system with phase-shifted PWM operating under the conditions of $m_{pv1} = m_{wind} = m_{pv2}$, $I_{pv1} = I_{wind} = I_{pv2}$, $f_{line} = 50$ Hz and $f_{sw} = 20$ kHz (top to bottom) i_1, i_2, i_3, i_{dc}, i_{inv}, v_{ac}, and i_{ac}.

modules in parallel with the other modules through their own DC-DC chopper to a common DC-bus. The configuration of multimodules PV/wind system with all modules connected in parallel is shown in Figure 18. The waveforms of the converter can be shown in Figure 19.

5. Conclusion

A grid-connected inverter for hybrid PV/wind power generation system was proposed. The proposed inverter was based on the current source inverter (CSI) topology. A number of issues were investigated, including the simple current sharing technique, the inverter configuration, operating principle, PWM strategy technique, PWM current analysis, and design consideration. The emphasis of this paper was on the new power converter scheme, where the operating analysis was discussed in details. The proficiency of the proposed inverter was accessed through the computer simulation under the different operation conditions. The performance of the proposed CSI was confirmed by the simulation results.

Acknowledgments

This work is supported in part by Thailand Research Fund (TRF) through the Royal Golden Jubilee Ph.D. program under Grant no. PHD/0166/2550, by the French Government's contribution to the RGJ-Ph.D program, and by the Energy Policy and Planning Office (EPPO), Ministry of Energy, Thailand. This work is also supported by National Research University (NRU) Project from Office of the Higher Education Commission of Thailand.

References

[1] Y. M. Chen, Y. C. Liu, S. C. Hung, and C. S. Cheng, "Multi-input inverter for grid-connected hybrid PV/wind power system," *IEEE Transactions on Power Electronics*, vol. 22, no. 3, pp. 1070–1077, 2007.

[2] C. Liu, K. T. Chau, and X. Zhang, "An efficient wind-photovoltaic hybrid generation system using doubly excited permanent-magnet brushless machine," *IEEE Transactions on Industrial Electronics*, vol. 57, no. 3, pp. 831–839, 2010.

[3] P. G. Barbosa, H. A. C. Braga, M. C. B. Rodrigues, and E. C. Teixeira, "Boost current multilevel inverter and Its application on single-phase grid-connected photovoltaic systems," *IEEE Transactions on Power Electronics*, vol. 21, no. 4, pp. 1116–1124, 2006.

[4] Y. Chen and K. Smedley, "Three-phase boost-type grid-connected inverter," *IEEE Transactions on Power Electronics*, vol. 23, no. 5, pp. 2301–2309, 2008.

[5] N. Vázquez, H. López, C. Hernández, E. Vázquez, R. Osorio, and J. Arau, "A different multilevel current-source inverter," *IEEE Transactions on Industrial Electronics*, vol. 57, no. 8, pp. 2623–2632, 2010.

[6] R. T. H. Li, H. S. H. Chung, W. H. Lau, and B. Zhou, "Use of hybrid PWM and passive resonant snubber for a grid-connected CSI," *IEEE Transactions on Power Electronics*, vol. 25, no. 2, pp. 298–309, 2010.

[7] B. M. T. Ho and H. S. H. Chung, "An integrated inverter with maximum power tracking for grid-connected PV systems," *IEEE Transactions on Power Electronics*, vol. 20, no. 4, pp. 953–962, 2005.

[8] G. Ertasgin, D. M. Whaley, N. Ertugrul, and W. L. Soong, "Implementation and performance evaluation of a low-cost current-source grid-connected inverter for PV applications," in *Proceedings of the IEEE International Conference on Sustainable Energy Technologies (ICSET '08)*, pp. 939–944, November 2008.

[9] M. Kazerani, Z. C. Zhang, and B. T. Ooi, "Linearly controllable boost voltages from tri-level PWM current-source inverter," *IEEE Transactions on Industrial Electronics*, vol. 42, no. 1, pp. 72–77, 1995.

[10] B. Bouneb, D. M. Grant, A. Cruden, and J. R. McDonald, "Grid connected inverter suitable for economic residential fuel cell operation," in *Proceedings of the European Conference on Power Electronics and Applications*, p. 10, September 2005.